Nuclear Instruments and Methods in Physics Research A 592 (2008) 346–353

Contents lists available at ScienceDirect

Nuclear Instruments and Methods in Physics Research A

journal homepage: www.elsevier.com/locate/nima

Detailed analysis of events from high-energy X-ray photons impinging on a two-phase front-illuminated CCD

T. Levato *,[1], L. Labate [2], M. Galimberti [3], A. Giulietti [2], D. Giulietti [1], L.A. Gizzi [2]

Intense Laser Irradiation Laboratory, IPCF, Consiglio Nazionale delle Ricerche, Pisa, Italy

ARTICLE INFO

Article history:
Received 14 April 2007
Received in revised form
1 April 2008
Accepted 8 April 2008
Available online 15 May 2008

PACS:
07.85.Nc
07.85.−m
29.40.Wk

Keywords:
Charge-coupled device
Cloud shape
X-ray spectrometer
Multi-pixel
Single-pixel
Single-photon

ABSTRACT

A study of the single-photon events generated by the interaction of X-rays up to 60 keV with a true two-phase charge coupled device (CCD) is reported. In particular, a relevant classification of the events is carried out according to their size and collected charge. This classification shows the occurrence of two main groups, characterized by a quite large difference in the ADU values that has been observed between events having different sizes but coming from photons with the same energy. Based upon 2D numerical calculations accounting for the charge cloud dynamics, diffusion and recombination, an explanation is suggested for this difference, arising from the difference in the electric field strength in the point of initial interaction. Moreover, the relative abundance of these two groups was found to be energy dependent. A model accounting for the true two-phase pixel structure was found to be a valid tool for a correct prediction of this abundance and an enhanced reconstruction of the spectra of the impinging photons.

1. Introduction

The use of CCD cameras has spread in the last years from astronomy [1] to other fields of fundamental and applied research [2], including, e.g., plasma physics [3–8], time-resolved X-ray diffraction [9], medical imaging [10] and nuclear physics [11,12]. In fact, CCDs are rapidly becoming the main tool in research laboratories for detecting electromagnetic radiation in the soft X-ray range, both for imaging and spectroscopic applications. This is mostly due to their ease-of-use as well as to other remarkable features such as linearity, high dynamic range and sensitivity.

As it is well known, the quantum efficiency (QE) of standard CCDs rapidly decreases for photon energies above 10 keV, due to the increasing photon attenuation length in Si, which overcomes the typical depletion thickness. As an example, the X-ray attenuation length in Si at a photon energy of 30 keV is 3 orders of magnitude higher than at 1 keV, causing a corresponding reduction in the QE. This circumstance led in the last years to a growing effort in producing CCDs with thicker depletion layers, which resulted in the appearance of the so-called Deep Depletion (DD) CCDs (see for example Refs. [13,14] and references therein).

However, standard CCD devices still retain their usefulness in order to detect high-energy (up to some tens of keV) X-ray photons in the case of high flux X-ray sources. An interesting case is when the CCD detector is used in the so-called single-photon detection regime. As it is known, this regime, relying on the fact that the total charge released by the interaction of an X-ray photon is basically proportional to its energy, allows the energy spectrum of the incoming radiation to be retrieved without any external dispersion device. In order for this mode of operation to give a spectral resolution as high as possible, an accurate knowledge of the CCD structure is required [15–17].

In general, the final charge collected after the readout process is actually the result of the primary charge cloud drift, diffusion and recombination across the CCD [18]. The size of the primary charge cloud depends primarily on the energy of the incoming photon [19]. However, due to the finite drift velocity, diffusion and recombination processes can have a significant effect on the final size and collected charge [18,20] depending on the electric field strength in the region of the initial interaction. As it is known, the

* Corresponding author. Present addresses: ILIL-IPCF (CNR), Area della Ricerca di Pisa, via Moruzzi 1, 56124 Pisa, Italy. or BIONEM Lab., Dipartimento di Medicina Sperimentale e Clinica, Università della Magna Graecia, Viale Europa 88100 Catanzaro, Italy. Tel.: +39 050 315 2256; fax: +39 050 315 2230.
E-mail address: tadzio.levato@df.unipi.it (T. Levato).
[1] Also at Dipartimento di Fisica, Università di Pisa and INFN, Sezione di Pisa, Italy.
[2] Also at Istituto Nazionale di Fisica Nucleare, Sezione di Pisa, Italy.
[3] Now at Central Laser Facility, Rutherford Appleton Laboratory, Chilton, Didcot, Oxfordshire, UK.

0168-9002/$ - see front matter © 2008 Elsevier B.V. All rights reserved.
doi:10.1016/j.nima.2008.04.011

electric field in the pixel volume is not uniform because of architecture requirements. In general, starting from the pixel surface, a first zone with a high electric field, the so called 'depletion zone', is present, followed by a region where the field decreases rapidly towards zero in the so called 'field-free zone'. Moreover, at a given depth, moving along directions parallel to the pixel surface, the field intensity may change in different ways depending on the specific readout technique [21]. The effects of the initial interaction position on the final spectrum, due to difference in the interaction depth, are well described in literature [22,23], as well as the Si escape peak [24]. The charge spreading between neighbour pixel due to different transversal positions at a fixed depth is also well addressed [25,26]. In the last years the so-called 'mesh technique' was introduced [27], allowing experimental studies about the charge cloud with sub-pixel resolution to be performed [28–31]. These studies clearly show that the charge cloud shape can provide a wealth of information about the primary interaction position [32] as well as about the polarization of the incoming photon [33]. When the initial interaction occurs in a zone with low electric field, diffusion effects increase and the final charge cloud can be much bigger than the initial one, giving rise to multi-pixel events. Thus, charge spreading between neighbouring pixel is of a major concern. In the case of low energy (up to 10 keV) X-ray photons, the presence of multi-pixel events is a direct indication of charge spreading. In fact the size of the initial charge cloud in this case is of the order of 1 μm (see Ref. [18] and reference therein), smaller than the typical pixelsize, 10 μm. In the case of high energy (up to 60 keV) X-ray photons, the multi-pixel events may be the most abundant occurrence, since the size of initial charge cloud in this case is greater than 10 μm.

Due to the fact that in multi-pixel events the retrieved charge may be significantly smaller than the total initial one, because of the greater importance of diffusion and recombination processes, a careful analysis is required in view of a correct spectral identification. In particular, it is very important to distinguish between different kinds of events for a correct calibration and counting. For this reason, using different X-ray monochromatic lines, we employ a detailed analysis on collected charge and event size, that enables us to understand the different spectroscopic features of single-pixel and multi-pixel events.

In this paper, we use the Pavlov model [18] for the analysis of the events generated by the interaction of high energy (i.e. higher than 10 and up to 60 keV) photons impinging on a conventional front-illuminated CCD device. The details about data acquisition and processing are given in Sections 2 and 3. We use a parametrization of the event size as a way to distinguish events generated by photons with the same energy but interacting in zones with different electric field strengths. By comparing two simple models for the geometry of the electric field inside the pixel, that provide the expected ratio between the single and multi-pixel events, with the experimental data, we were able to show some features related to the specific 'true two-phase' readout technique [21]. On the basis of 2D numerical calculations, using such a shape of the electric field, we could recognize the effects due to different initial interaction positions. This analysis highlights the need for different energy calibrations based upon a selection of the different kinds of events as produced by this particular architecture.

2. Data acquisition

The study has been carried out using a commercially available, true two-phase, front-illuminated CCD chip (Kodak KAF 0261) equipped with a 15 μm thick Be window. This full-frame, buried channel CCD consists of 512×512, $20 \times 20\,\mu m^2$ wide, pixels. During the acquisitions the chip was kept at an operating temperature of $-5\,^{\circ}C$ by means of a Peltier device. All the data discussed below refer to three different sets of acquisitions, two of them obtained with a continuous source and the last with a pulsed source. The first two data sets are relative to a ^{241}Am radioactive source used in combination with a set of metal foils, used both as attenuators and as secondary sources of fluorescence lines. The third data set is relative to a laser-plasma based X-ray source; we will refer to this data set as 'pulsed data'. This source is based on the 2TW Ti:Sa laser system, delivering 130 mJ in 65 fs, operating at the ILIL laboratory at the CNR Campus in Pisa. The laser beam was focused by an $f/4$ parabolic mirror in a 10 μm diameter (FWHM) spot on a 12 μm thick Ti target. The X-ray radiation obtained from this source consists primarily of the $TiK_{\alpha,\beta}$ fluorescence emission and is characterized by a very short duration, smaller than 1 ps (see Ref. [34] for details on the laser system and X-ray source). In Table 1 we summarize the main emission lines of ^{241}Am and fluorescence emissions of the used metal foils, with the corresponding relative intensity and the CCD QE (relative to a 20 μm thick layer).

Table 1
Photon energy, relative intensity (if available and/or applicable) and corresponding CCD efficiency (relative to a 20 μm thick layer) for the lines used in our study, coming from either the ^{241}Am radioactive source or from secondary fluorescence sources

Emission line	Energy (keV)	Relat. intens.	CCD efficiency
$Np_{L\alpha}$	13.9	37%	0.06
$Np_{L\beta}$	17.7	n.a.	0.03
$Np_{L\gamma}$	21.0	n.a.	0.02
^{241}Am-γ	26.3	2%	0.01
^{241}Am-γ	59.6	36%	0.001
SK_{α}	2.30	n.a.	~1
TiK_{α}	4.51	n.a.	0.8
CuK_{α}	8.05	n.a.	0.3

3. Data analysis

All the acquisitions used strictly fulfilled the single photon condition (that is, the photon flux was sufficiently low to avoid pileup). After the subtraction of an unexposed image acquired under identical settings (in order to account for eventual chip specific pattern, hot pixels, etc.), the analysis algorithm looks for all the pixels above a predefined ADU threshold (typically chosen at $3w_B$, being w_B the HWHM of the background pulse height distribution) and among these one seeks the local maxima. An *event* is then defined starting from each of these local maximum pixels and selecting a suitable pixel range around that. The analysis of each event is carried out according to the Pavlov model [18] for the collected charge over the CCD pixel. According to this model, the final charge cloud is assumed to have a 2D gaussian distribution over the chip surface (x–y plane), normalised to the total charge Q_0 and with variances σ_x, σ_y along the two orthogonal directions x, y. The charge Q_{ij} collected in each pixel ij corresponds to the integral of this function over the pixel surface. The analysis minimizes the sum of the quadratic differences between the value Q_{ij} and the experimental value ADU_{ij} of each pixel involved in the event, using a modified simplex algorithm (see for example Ref. [35]) with the following initial parameters:

- $Q_0^{(ini)}$ is the total ADU of the event, calculated as the sum of the levels of its pixels;
- $\sigma_{x,y}^{(ini)}$ are proportional to the width of the event in pixels;

- $x_0^{(ini)}, y_0^{(ini)}$ are the coordinates of the center of the most intense pixel.

Finally, we observe here that we denoted with x the direction of the channel stops (in other words, the charge shift during the readout process occurs along x). In the following, the z coordinate will be used too, in the direction perpendicular to the CCD surface.

4. Event size distribution and discussion

Using the parameters resulting from the data analysis, the events can be classified according to their energy and/or size. As it is well known, different sizes mean, generally speaking for fixed photon energy, different diffusion effects. Furthermore, if we restrict our attention to photons interacting in the depletion region, the Pavlov model predicts that the final charge cloud radius r_d is related to the primary photon interaction depth z by the expression $r_d \propto \log(d/(d-z))^{1/2}$, being d the depletion depth ($z<d$). In our case, we used the area of the events $\xi = \sigma_x\sigma_y$ as an event classification parameter, which, according to this model, is directly related to the interaction depth. The use of such a parameter was suggested by the structure of the event distribution in the $\xi - Q_0$ plane. This approach can be checked by looking at Fig. 1 showing the event distribution for the events coming from the TiKα (~410ADU) and Kβ (~450ADU) lines: actually, the two lines can only be resolved for the events with $\xi<10^{-2}$; however, in what follows we will refer generally to the Kα events, since Kβ events are a small fraction ($\sim 10^{-1}$) of these ones. According to this plot, besides some events homogeneously distributed, two well-defined groups (which we will refer to throughout this paper as *kinds* or *groups*) can be identified, corresponding to the same emission line, in this case the TiKα line (see also Fig. 3, where two main peaks for each emission line are visible). In particular, a first group can be identified with $\xi \leqslant 2\times 10^{-2}$. We will refer to these events as *small*. A second group is defined by $\xi \geqslant 10^{-1}$ (from now on *large* events). We point out here that the parameter ξ was used in our analysis only for distinguishing between these two, well-separated groups by using suitable threshold values. Hence, the errors on the σ_x, σ_y values (which are greater, in particular, in the case of small events) do not affect our conclusion. As a first, general observation we can guess that the first kind of events can be related to photons interacting in the depleted zone, so that the short collection time accounts for the *small* size, and the second one is due to interactions into zones where a smaller electric field accounts for a longer collection time and a smaller collected charge. However, as it will be shown later, this kind of events do not come from interactions that are too deep in the undepleted bulk, as this would lead to a greater charge loss than the one observed (see Section 6 for a more quantitative discussion). Fig. 2 shows the pulse height distributions for the two kind of events. The pulse height distribution relative to single-pixel events is also shown, which comes out to be very similar to that of small events, as expected. It is worth noting here that the *small* and *large* event distributions are peaked at different ADU. The TiKα case shows a difference of about 60 ADU, that is about 15% of the collected charge; in general it was less than 20% in the energy range considered in this paper. Finally, we observe that a similar behaviour as that of the TiKα line was observed for the other considered lines as well (though with a different ratio between the number of events in the two groups, see Fig. 3), demanding for the two groups of events to be considered in different ways for the sake of the spectrum reconstruction. We observe here that (a) the above behaviour holds both for radioactive and for the laser-plasma source 'pulsed data'; since

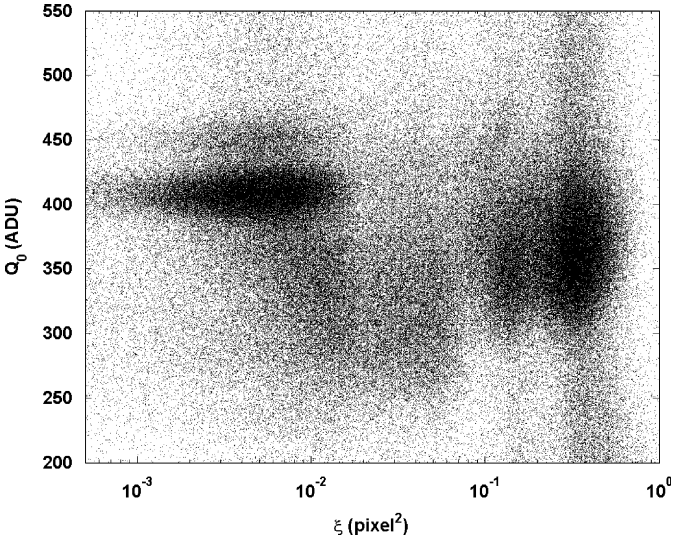

Fig. 1. Event distribution in the ξ–Q_0 plane for the TiK$_\alpha$ and K$_\beta$ lines.

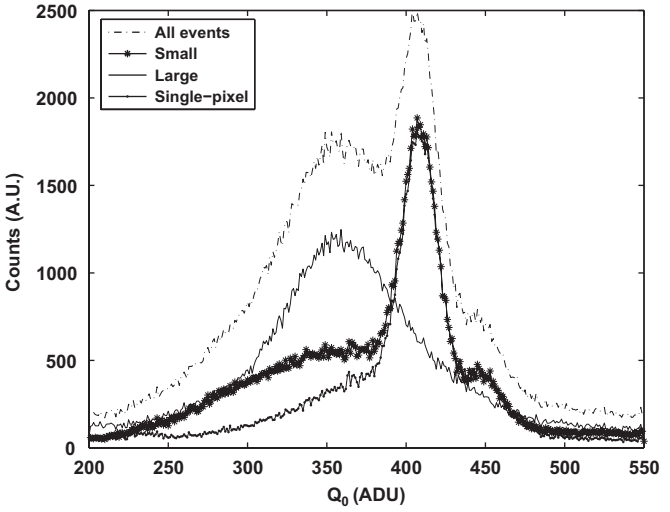

Fig. 2. Pulse height distributions for the *small*, *large* (see text), single-pixel and all the events relative to the same data set as in Fig. 1.

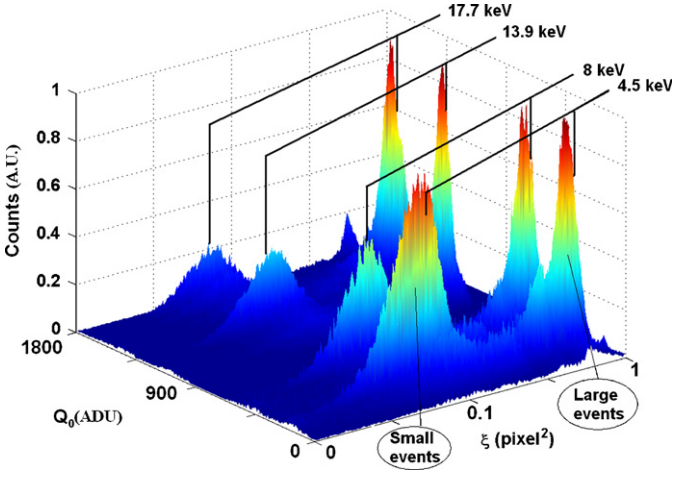

Fig. 3. (colour online) 3D view of the event distributions in the ξ–Q_0 plane for different lines. Each distribution is normalized to the maximum counts of the corresponding large events.

the duration of the X-ray emission in this latter case is much smaller than the integration and readout times, we can definitely conclude that the presence of the two groups cannot be related to photons hitting the CCD during the readout time; (b) the physics which is going on in the channel stops, which has been found in previous works to result in different collected charge with respect to the one in the depleted regions, cannot account for the relative number of events of the two groups. As it will come out in the next section, the true two-phase architecture plays a fundamental role in this behaviour. A first step toward this conclusion can be made by looking at the ratio R_{sl} of the number of small to large events as a function of the photon energy. Fig. 3 shows a 3D view of the distribution on the $\xi - Q_0$ plane for the X-ray lines at 4.5, 8, 13.9, 17.7 keV (for each line, the normalization of the corresponding counts is to the peak of the *large* event distribution). Table 2 summarizes the R_{sl} values gained from our analysis for different photon energies, as well as the corresponding photon attenuation length and the average initial charge cloud radius calculated according to $R_0(\mu m) = 0.012\,E^{1.75}(keV)$ [18]. As shown in Fig. 3, the number of *small* events decreases rapidly with energy, vanishing

Table 2
Ratio R_{sl} of the number of *small* to *large* events as obtained by our analysis for different emission lines

Energy (keV)	2.30	4.51	8.05	13.9	17.7	21.0	26.3	59.6
R_{sl}	∞	0.99	0.52	0.47	0.33	0.25	0.20	0
Att. Length(μm)	2.2	13.5	70.5	355	704	1190	2064	13 000
R_0(μm)	0.05	0.17	0.45	1.2	1.8	2.5	3.6	16

The corresponding photon attenuation length in Si and expected charge cloud radius is also reported.

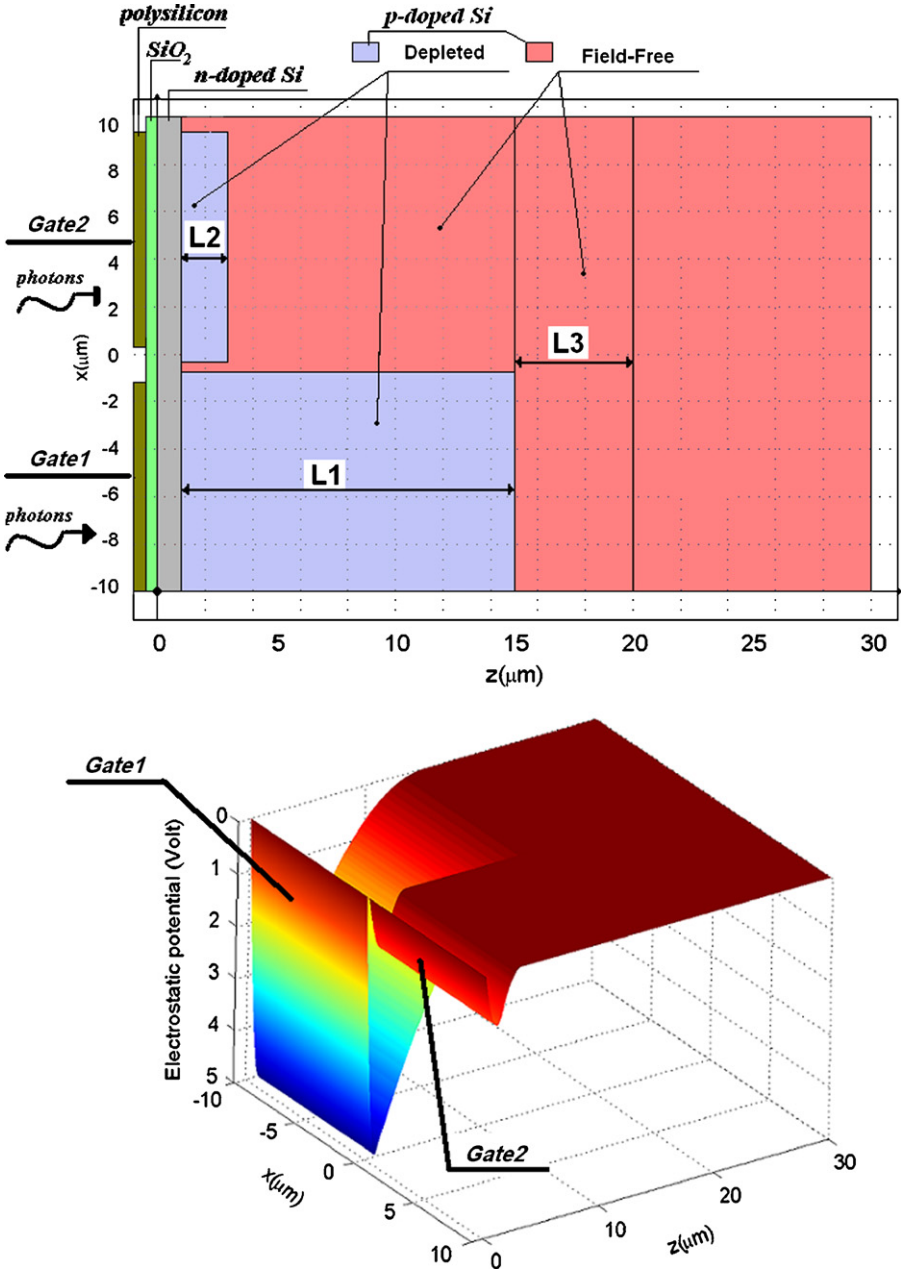

Fig. 4. (colour online) *Top*: schematic view of the true two-phase pixel structure (gate and SiO_2 not in scale), where the used thicknesses of the two depleted zones (L_1, L_2) and of the field-free zone (L_3 starts from the end of L_1) have been indicated. *Bottom*: electrostatic potential used in our calculations.

for energies above 30 keV. This behaviour is also visible in Table 2. According to Table 2, at a photon energy of 2.3 keV only *small* events are present, thus suggesting that these low energetic photons do not reach the zone with a lower electric field. In the following Section we show that the information collected so far can be used to obtain some indication on the electric field structure inside the pixel volume.

5. Pixel structure and effect on the event distribution

Because of the specific readout technique of our CCD chip, the so-called 'true two-phase' technique, two different voltages are applied to the two gates of each pixel, resulting in two different electrostatic potential behaviours in the two halves of the pixel volume (see Ref. [21] for details in our case). For the sake of the visualization, Fig. 4 *top* shows a schematic view of the geometry of a true two-phase pixel in the z (normal to the CCD surface) and x (readout, see above) directions. The typical sizes of the two depletion zones are also sketched.

Assuming that small events originate from photons interacting in depleted zones and large events from photons interacting in zones with lower electric field, it is possible to predict the expected ratio R_{sl} versus photon energy, using the known attenuation length in Si and the volumes of the different zones. Although not sensitive to the detailed behaviour of the electrostatic potential *inside* a depleted zone (only the zone sizes are important here), this model allows the observed ratio R_{sl} to be fitted quite well on all considered energy range. The radius of the initial charge cloud must also be taken into account in the R_{sl} modelling, considering it on the borders of the considered volumes. Fig. 5 shows the expected ratios of R_{sl} as a function of energy (curve Model 1a) for a 2 gate pixel structure as the one showed in Fig. 4 (*top*) with the values $L_1 = 15\,\mu m$, $L_2 = 3\,\mu m$. The experimental data presented in Table 2, with an error of 10% on each measured quantity, are also shown. For the comparison, the expected behaviour assuming a 'uniform' pixel (i.e., with $L_2 = L_1 = 15\,\mu m$) is also shown (model 2a), as well as the corresponding curves when no account is made in the model for the finite initial charge cloud radius. As expected, this leads to an overestimate of the ratio at high energies. In all the four considered cases, the thickness of the field-free region L_3, was obtained to be less than half of the diffusion length in one recombination time, $L_3 \sim \frac{1}{2}\sqrt{4 \cdot D \cdot t_{ric}} \sim 5\,\mu m$. Indeed, as it will be shown in the next section, photons interacting deeper in the pixel suffer from a charge loss bigger than the one observed for the *large*event group, thus giving no contribution to the observed ratio R_{sl}. As it can be seen from Fig. 5, our model of the two-phase architecture predicts quite well the observed ratio over the whole considered energy range when the potentials (or, more properly here, the thicknesses of the different zones) are chosen as in Fig. 4 (see *bottom* for more details).

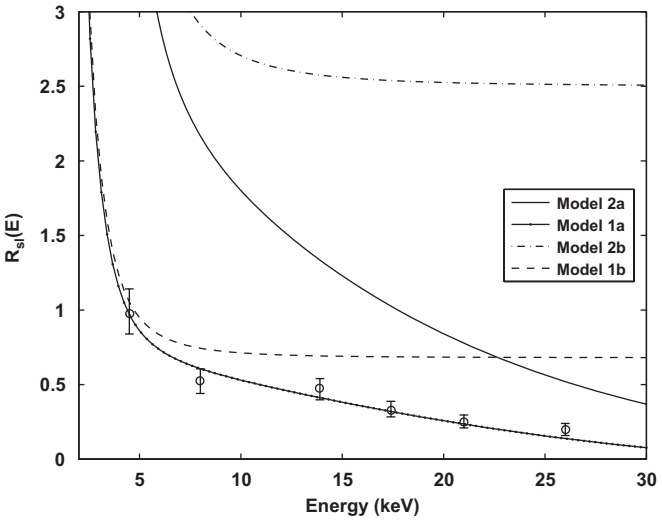

Fig. 5. Expected behaviour of the ratio of the number of *small* to *large* events as calculated assuming that *small* events originate from photon interactions in the depleted zones and *large* ones from interactions in the field-free zones. 1a, 1b: two-phase structure (i.e., two different potentials under the two gates), with (a) and without (b) account for the finite initial charge cloud radius (i.e., infinitely small one); 2a, 2b: same as for 1a,1b, but with the same potential under the two gates (that is, considering a 'one-gate-like' pixel with $L_1 = L_2 = 15\,\mu m$). The experimental data for R_{sl} are also shown.

6. 2D numerical calculation

Based upon the model of the pixel structure discussed and validated in the previous section, we can estimate from analytical considerations the expected difference in the final collected charge between the two groups of *small* and *large* events and compare that with the observed one. This can be made by considering the diffusion equation governing the evolution of the charge cloud $\rho(x,z,t)$ in the plane x–z, namely [36]

$$\frac{\partial \rho}{\partial t} = D\nabla^2\rho - \frac{\rho}{\tau_{eff}} - \vec{v}\cdot\vec{\nabla}\rho \qquad (1)$$

Here

- D is the diffusion coefficient;
- $\tau_{eff} = \frac{\tau_r}{(1+\tau_r\,\vec{\nabla}\cdot\vec{v})}$, with τ_r electron-hole recombination time and $\vec{v}(x,z) = -\mu\vec{E}(x,z)$, being $\mu = eD/k_BT$ the electron mobility and $\vec{E}$ the electric field experienced by the electrons.

The initial charge cloud was assumed to be Gaussian with a mean squared radius given by R_0 [18] as indicated in Section 4. The equation was solved numerically for different photon energies. The electrostatic potential used for numerical calculation is shown in Fig. 4. The following values for the diffusion coefficient D and the recombination time τ_r were used: $D = 25\,cm^2/s$, $\tau_r = 2.5 \times 10^{-8}$ s. Each electron was considered as 'collected' once it arrived at the position of the minimum potential (which means that no account has been taken of the recombination occurring on long time scales, comparable to the acquisition time). Fig. 6 shows the ratio of the collected charge to the initial released charge, for two different X-ray photon energies, as a function of the primary interaction depth z inside the pixel. Different curves are shown, relative to different x positions (see Fig. 4). As expected, the collected charge decreases rapidly out of the depletion zones. This is why only a small part of the undepleted bulk (L_3) was obtained by fitting the experimental data of R_{sl} with the model presented in the previous section: photons interacting too much in depth are affected by a charge loss bigger than 20% and are present on spectra as a continuum extending towards very low collected charge, so that they are not included in the selection used for the evaluation of R_{sl}. The effect of charge loss is greater at lower energies than at higher ones, due to the fact that the initial charge cloud in the latter case extends over a longer distance, therefore averaging the collected and lost charge. Fig. 7 shows the ratio of the collected charge to the initial released charge as a function of the primary photon landing position along the x direction (curves corresponding to different values of z are shown). Although being a simplified description of the actual situation, the difference in

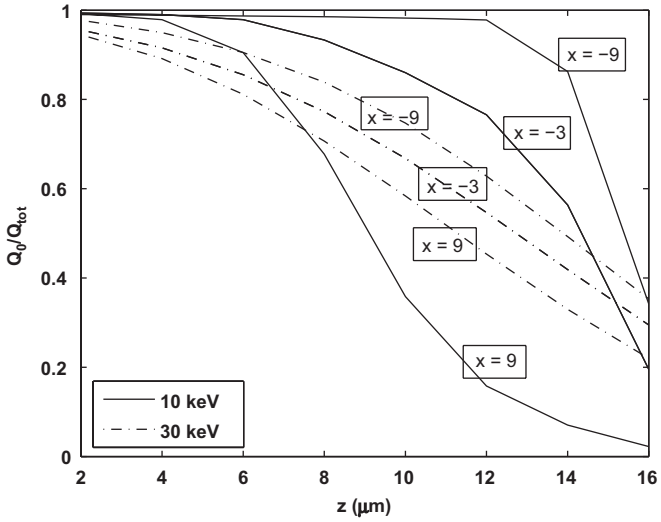

Fig. 6. Ratio of the collected charge to the initial released charge, for two different X-ray photon energies, as a function of the primary interaction depth inside the pixel. Curves corresponding to different x positions are shown (see Fig. 4 *top*).

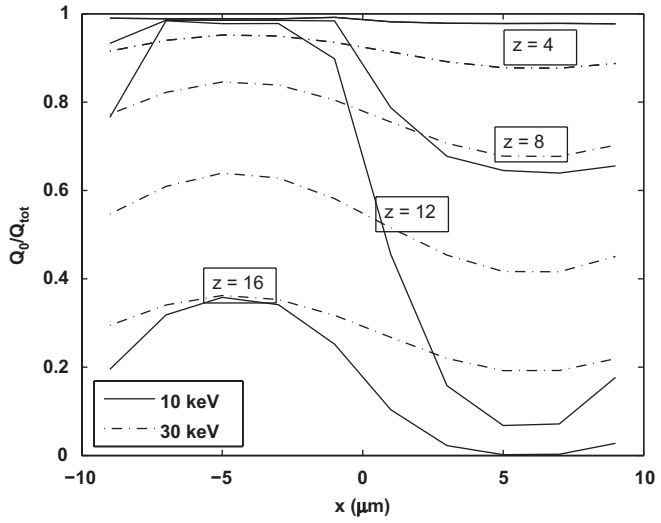

Fig. 7. Ratio of the collected charge to the initial released charge as a function of the primary photon landing position in the transverse pixel direction. Curves relative to different z positions are shown (see Fig. 4 *top*).

the final collected charge between photons interacting inside the two different depleted half-pixels (see for example Fig. 7, curve with $z = 8$) shows a maximum charge loss of some tens percent, thus very similar to the experimental one between events belonging to the two distinct groups in Fig. 1.

7. High energy spectrum

From the above considerations, it is clear that events belonging to the two different groups of Fig. 1 should be considered separately for the sake of the spectrum reconstruction, due to the difference in their resulting collected charge. Moreover, besides the QE of the detector, it is clear that the different probabilities for a photon at a given energy to be detected as a small or large event should be possibly taken into account. Indeed, the QE accounts for all the intercepted photons without distinction between *small* and *large* events, but, as shown in Fig. 3, these two groups have different behaviour with energy. Our study enables us to use the pixel structure as resulting from the model described in Section 5 for a separate estimate of the QE for these two groups. We therefore introduce an effective Quantum Efficiency (eQE) which, beside to the dependence of the attenuation length on the photon energy, accounts for the geometrical factor affecting *small* and *large* events in a different manner. In particular, while the QE is related to a 'one-gate-like' pixel (see *Model 2a* in Fig. 5 and Section 5) and is calculated considering the active volume, the eQE_{small} and eQE_{large} are calculated by considering the primary photon interaction probability in each different region of the detailed structure of the two-gate pixel (see Section 5). Fig. 8 shows (a) the spectrum of the *small* events up to 30 keV (no signal was present above this energy for *small* events), (b) the spectrum of *large* events up to 30 keV, (c) the spectrum of *large* events from 25 to 70 keV, and (d) the eQE for both the *small* and *large* events, as obtained for the pixel structure described in Section 5. As suggested by the numerical calculation in the previous section, when the photon energy increases a reduction of the resolution occurs (see Fig. 8(c), emission lines at 26 and 60 keV) as a consequence of the 'smearing' of the charge cloud over different regions inside the pixel volume. The effect is particularly important in our two-gate structure pixel, as the smearing occurs over different regions both in the z and x directions. The FWHM was estimated to be about 150 eV for *small* events and about 2 keV for *large* events. Finally Fig. 9 shows the spectra obtained considering QE for all the events and the spectra obtained considering the eQE_{small} for *small* events and eQE_{large} for *large* events. According to this plot, there is a significant difference between the corrected (with eQE) and uncorrected (that is, corrected with the simple QE) spectra. The emission lines at 13.9 and 59.9 keV, for example, exhibit a measured integral ratio of ~0.9 that agrees well with the expected one ~1 only in the case of *eQE*-corrected spectra.

8. Summary and conclusions

We reported on a detailed analysis of the events resulting from high energy (up to 60 keV) photon interactions with a conventional true two-phase front-illuminated CCD device. The analysis was mainly aimed at studying the distribution of the event size as a function of the energy and interaction position inside the pixel volume. Our analysis clearly shows the presence of two different and well-separated groups of events in the ξ–Q_0 plane. The two groups give rise to different values of the ADU (i.e. collected charge) corresponding to the same X-ray photon energy. This can be explained by considering the detailed structure of the pixel for this architecture. Indeed, the ratio of the number of *small* to *large* events was found to be well predicted by a model accounting for the two gate structure. Based upon this model, a numerical solution of the diffusion equation in two dimensions was obtained. This allowed to highlight the observed difference in the collected charge for the two groups of events, which was found to arise from the different electric field of the primary interaction position. Furthermore, a corrected, separate QE was introduced, taking into account the difference in the QE for the two groups due to the detailed pixel structure. From a practical viewpoint, in the case of single photon spectroscopy the result of this detailed analysis strongly suggests that the use of two different energy calibrations allows the final output to be improved, thus extending the spectral range of validity of the single photon spectroscopy, as well as the need to take into account two different quantum efficiencies for different counting of *small* and *large* events. These circumstances show the possibility of introducing

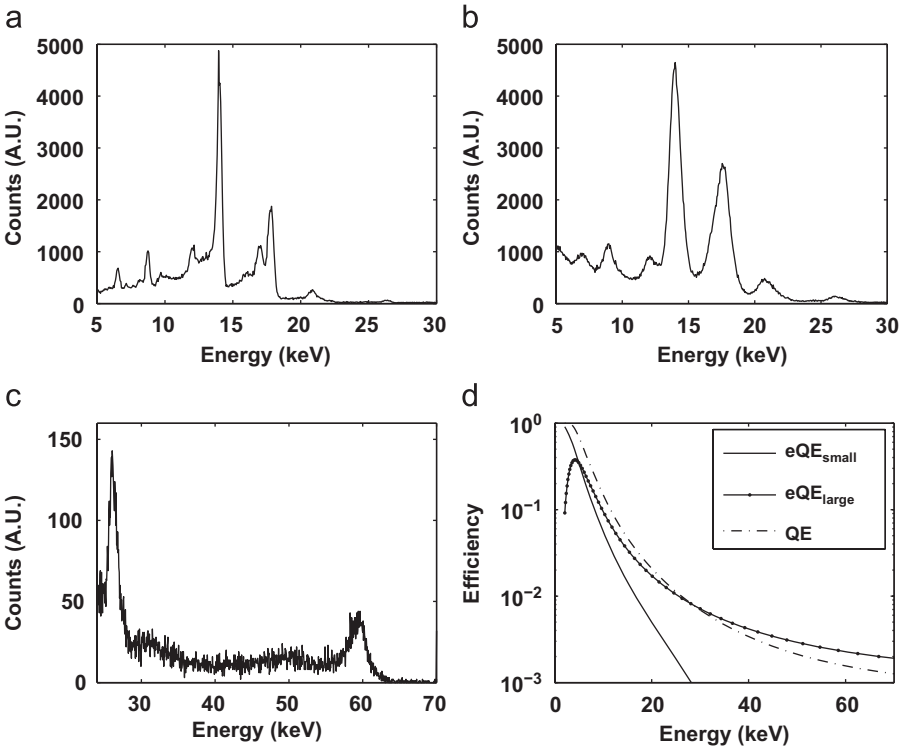

Fig. 8. Energy spectra of (a) *small* events up to 30 keV, (b) *large* events up to 30 keV, (c) *large* events from 25 to 70 keV, (d) Quantum Efficiency (QE) and effective Quantum Efficiency (eQE) for *small* and *large* events, as calculated for a pixel as the one in Fig. 4.

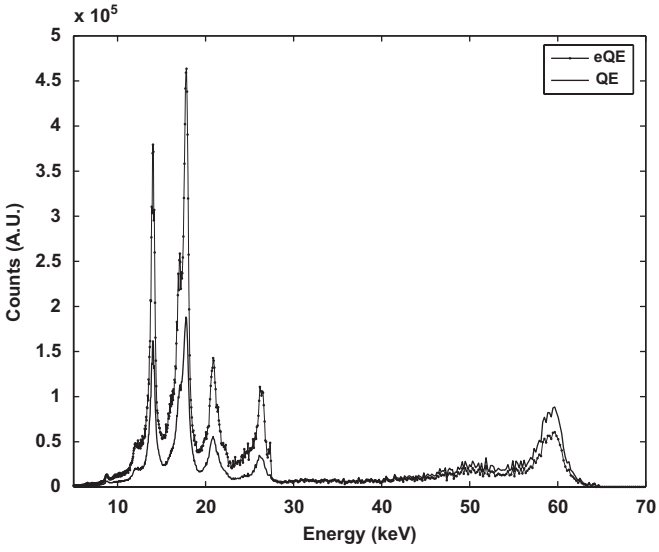

Fig. 9. Energy spectrum of an ^{241}Am source obtained considering both the *small* and *large* events and correcting the raw counts of the two groups with the same quantum efficiency (QE) and with different effective quantum efficiencies (eQE).

an *effective QE* to account for the detailed structure of the detector.

Acknowledgements

The authors wish to acknowledge support by the Italian MIUR projects FSSRIS 'Impianti Innovativi Multiscopo per la Produzione di Radiazione X e Ultravioletta', FIRB 'SPARX' and 'BLISS-Broadband Laser for ICF Strategic Studies' and by the INFN project 'PlasmonX'.

References

[1] G.W. Fraser, Nucl. Instr. and Meth. A 471 (2001) 170.
[2] S.M. Gruner, M.W. Tate, E.F. Eikenberry, Rev. Sci. Instr. 73 (2002) 2815.
[3] L.A. Gizzi, A. Giulietti, D. Giulietti, P. Köster, L. Labate, T. Levato, F. Zamponi, A. Lübcke, T. Kämpfer, I. Uschmann, E. Förster, A. Antonicci, D. Batani, Plasma Phys. Controll. Fusion 49 (2007) B211.
[4] L. Labate, A. Giulietti, D. Giulietti, P. Köster, T. Levato, L.A. Gizzi, F. Zamponi, A. Lübcke, T. Kämpfer, I. Uschmann, E. Förster, Rev. Sci. Instr. 78 (2007) 103506.
[5] F. Zamponi, T. Kämpfer, A. Morak, I. Uschmann, E. Förster, Rev. Sci. Instr. 76 (2005) 116101.
[6] L. Labate, M. Galimberti, A. Giulietti, D. Giulietti, P. Köster, P. Tomassini, L.A. Gizzi, Appl. Phys. B 86 (2007) 229.
[7] L. Labate, M. Galimberti, A. Giulietti, D. Giulietti, L.A. Gizzi, P. Tomassini, G. Di Cocco, Nucl. Instr. and Meth. A 495 (2002) 148.
[8] I. Uschmann, P. Gibbon, D. Klöpfel, T. Feurer, E. Förster, P. Audebert, J.P. Geindre, J.C. Gauthier, A. Rousse, C. Rischel, Laser Part. Beams 17 (1999) 671.
[9] A. Rousse, C. Rischel, S. Fourmaux, I. Uschmann, S. Sebban, G. Grillon, Ph. Balcou, E. Förster, J.P. Geindre, P. Audebert, J.C. Gauthier, D. Hulin, Nature 410 (2001) 65.
[10] J.E. Lees, G.W. Fraser, A. Keay, D. Bassford, R. Ott, W. Ryder, Nucl. Instr. and Meth. A 513 (2003) 23.
[11] M. Cargnelli, H. Fuhrmann, M. Giersch, A. Gruber, A. Hirtl, T. Ishiwatari, P. Kienle, J. Marton, J. Zmeskal, Nucl. Instr. and Meth. A 535 (2004) 389.
[12] T. Ishiwatari, G. Beer, A.M. Bragadireanu, M. Cargnelli, C. Curceanu, J.P. Egger, Nucl. Instr. and Meth. A 556 (2006) 509.
[13] T.M.V. Bootsma, E.J. van Zwet, A.G. Brinkman, J.W. den Herder, L. de Jong, P. de Korte, S.M. Olsthoorn, Nucl. Instr. and Meth. A 439 (2000) 575.
[14] B.E. Burke, J.A. Gregory, A.M. Loomis, M. Lesser, M.W. Bautz, S.E. Kissel, D.D. Rathman, R.M. Osgood, M.J. Cooper, T.A. Lind, G.R. Ricker, IEEE Trans. Nucl. Sci. NS-51 (2004) 2322.
[15] G.W. Fraser, A.F. Abbey, A.D. Holland, K.J. McCarthy, A. Owens, A. Wells, Nucl. Instr. and Meth. A 350 (1994) 368.
[16] M.W. Bautz, G.Y. Prigozhin, M.J. Pivovaroff, S.E. Jones, S.E. Kissel, G.R. Ricker, Nucl. Instr. and Meth. A 436 (1999) 40.

[17] L.K. Townsley, P.S. Broos, G. Chartas, E. Moskalenko, J.A. Nousek, G.G. Pavlov, Nucl. Instr. and Meth. A 486 (2002) 716.
[18] G.G. Pavlov, J.A. Nousek, Nucl. Instr. and Meth. A 428 (1999) 348.
[19] J.R. Janesick, Scientific Charge-Coupled Devices, SPIE Press Book, 2001.
[20] G.R. Hopkinson, Nucl. Instr. and Meth. A 216 (1983) 423.
[21] ⟨http://www.kodak.com/ezpres/business/ccd/global/plugins/acrobat/en/supportdocs/chargeCoupledDevice.pdf; http://www.kodak.com/US/en/digital/pdf/bluePlus.pdf; http://www.kodak.com/US/en/digital/pdf/ccdTerminology.pdf⟩.
[22] G. Prigozhin, N.R. Butler, S.E. Kissel, G.R. Ricker, IEEE Trans. Electr. Dev. ED-50 (2003) 246.
[23] G. Prigozhin, S. Jones, M. Bautz, G. Ricker, S. Kraft, Nucl. Instr. and Meth. A 439 (2000) 582.
[24] K.J. McCarthy, A. Owens, A. Keay, Nucl. Instr. and Meth. A 384 (1997) 403.
[25] R.F. Fowler, J.V. Ashby, C. Greenough, Nucl. Instr. and Meth. A 450 (2000) 75.
[26] R.F. Fowler, J.V. Ashby, C. Greenough, Nucl. Instr. and Meth. A 477 (2002) 226.
[27] H. Tsunemi, K. Yoshita, S. Kitamoto, Jpn. J. Appl. Phys. 36 (1997) 2906.
[28] H. Tsunemi, J. Hiraga, K. Yoshita, K. Hayashida, Nucl. Instr. and Meth. A 421 (1999) 90.
[29] H. Tsunemi, J. Hiraga, K. Yoshita, E. Miyata, M. Othani, Nucl. Instr. and Meth. A 439 (2000) 592.
[30] M. Pivovaroff, S. Jones, M. Bautz, S. Kissel, G. Prigozhin, G. Picker, H. Tsunemi, E. Miyata, IEEE Trans. Nucl. Sci. NS-45 (1998) 164.
[31] J.S. Hiraga, H. Tsunemi, Nucl. Instr. and Meth. A 562 (2006) 241.
[32] H. Tsunemi, J. Hiraga, E. Miyata, Nucl. Instr. and Meth. A 477 (2002) 155.
[33] H. Tsunemi, Nucl. Instr. and Meth. A 541 (2005) 295.
[34] L.A. Gizzi, A. Giulietti, D. Giulietti, P. Köster, L. Labate, T. Levato, F. Zamponi, T. Kämpfer, I. Uschmann, E. Förster, R. Sauerbrey, in: SPIE Proceedings, vol. 6634, 2007.
[35] W.H. Press, S.A. Teukolsky, W.T. Vetterling, B.P. Flannery, Numerical Recipes in C, Cambridge University Press, New York, 1997.
[36] J.D.E. Beynon, D.R. Lamb, Charge-Coupled Devices and Their Applications, McGraw-Hill, New York, 1980.